nature

SUPPLEMENTARY INFORMATION

https://doi.org/10.1038/s41586-018-0550-z

In the format provided by the authors and unedited.

Ferroelectric polymers exhibiting behaviour reminiscent of a morphotropic phase boundary

Yang Liu[1], Haibibu Aziguli[1], Bing Zhang[2], Wenhan Xu[1], Wenchang Lu[2], J. Bernholc[2] & Qing Wang[1]*

[1]Department of Materials Science and Engineering, The Pennsylvania State University, University Park, PA, USA. [2]Department of Physics, North Carolina State University, Raleigh, NC, USA. *e-mail: wang@matse.psu.edu

SUPPLEMENTARY INFORMATION

Ferroelectric Polymers Exhibiting Behaviour Reminiscent of A Morphotropic Phase Boundary

Yang Liu,[1] Haibibu Aziguli,[1] Bing Zhang,[2] Wenhan Xu,[1] Wenchang Lu,[2] J. Bernholc,[2] Qing Wang[1]

[1]Department of Materials Science and Engineering, The Pennsylvania State University, University Park, PA 16802 USA

[2]Department of Physics, North Carolina State University, Raleigh, NC 27695-75188202, USA

Table of Contents

1. Nuclear magnetic resonance spectra

The P(VDF-TrFE) copolymers with the VDF content ranging from 45 mol% to 80 mol% were characterized by nuclear magnetic resonance (NMR) spectroscopy. The ^{1}H and ^{19}F NMR spectra are shown in Figures S1 and S2-S3, respectively. The ^{1}H NMR spectra were used to determine the molar ratio between VDF and TrFE. The assignments of the ^{19}F NMR signals of P(VDF-TrFE)s can be found in Extended Data Figure 2.

We compare the chain tacticity and piezoelectric responses between the synthesized and commercial copolymers (Figure S4 and Table S1). P(VDF-TrFE) purchased from Piezoetch Arkema and Solvey has the composition of 65/35 mol%. We characterized the purchased polymers along with the synthesized sample by NMR spectroscopy and strain-electric field measurements (Figure S24). As shown in Figure S4, the commercial samples present nearly the same ^{1}H and ^{19}F NMR spectra as our synthesized polymer. Moreover, our quantitative results indicate that all three polymers show nearly the same regio- and stereo-sequences (Table S1). Specifically, we find that the commercial samples possess only a slightly lower regiodefect (H-H/T-T) content than our synthesized sample and nearly the same chain tacticity distributions as our synthesized sample. On the other hand, we observe that all three P(VDF-TrFE) 65/35 mol% copolymer films have the same d_{33} value of ~-30 pC N^{-1}measured from the strain-electric field at room temperature (Figure S24). These results demonstrate that our synthesized copolymers are almost identical to the commercial samples in terms of the chemical microstructure and piezoelectric responses.

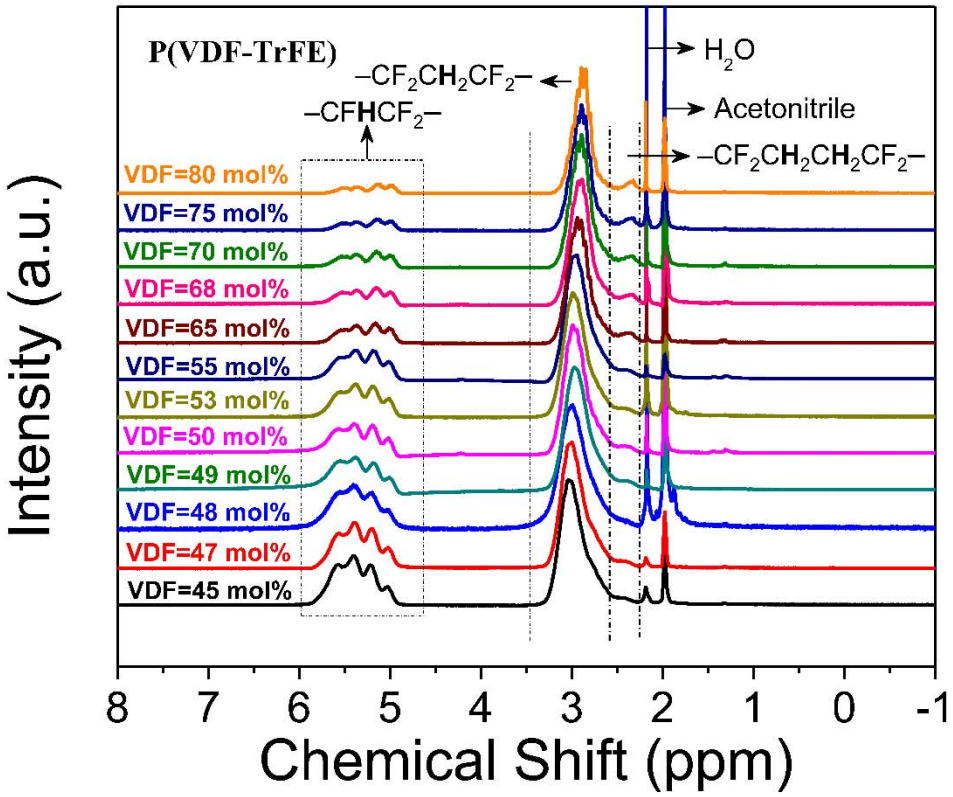

Figure S1. **^{1}H NMR spectra of the P(VDF-TrFE) copolymers with varying VDF contents.**

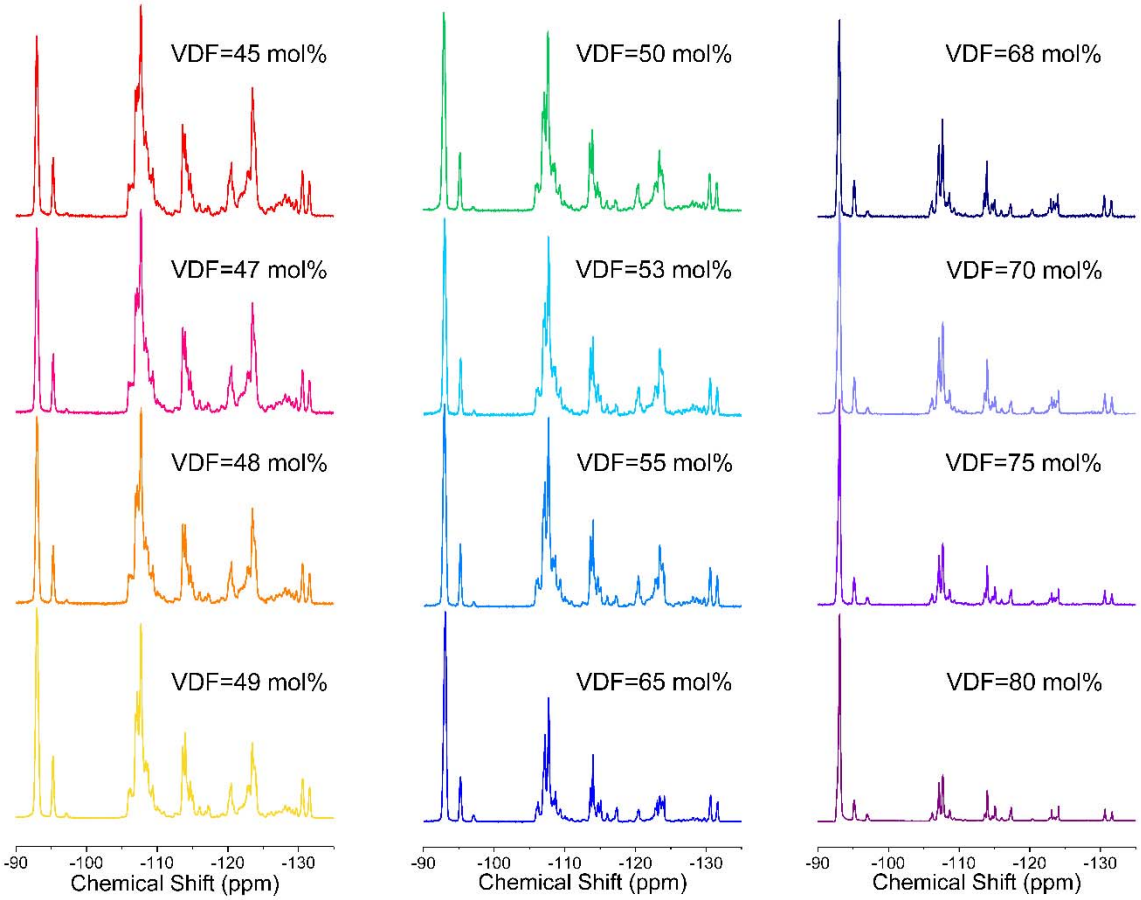

Figure S2. ^{19}F NMR spectra of the P(VDF-TrFE) copolymers in the region between -90 and -135 ppm.

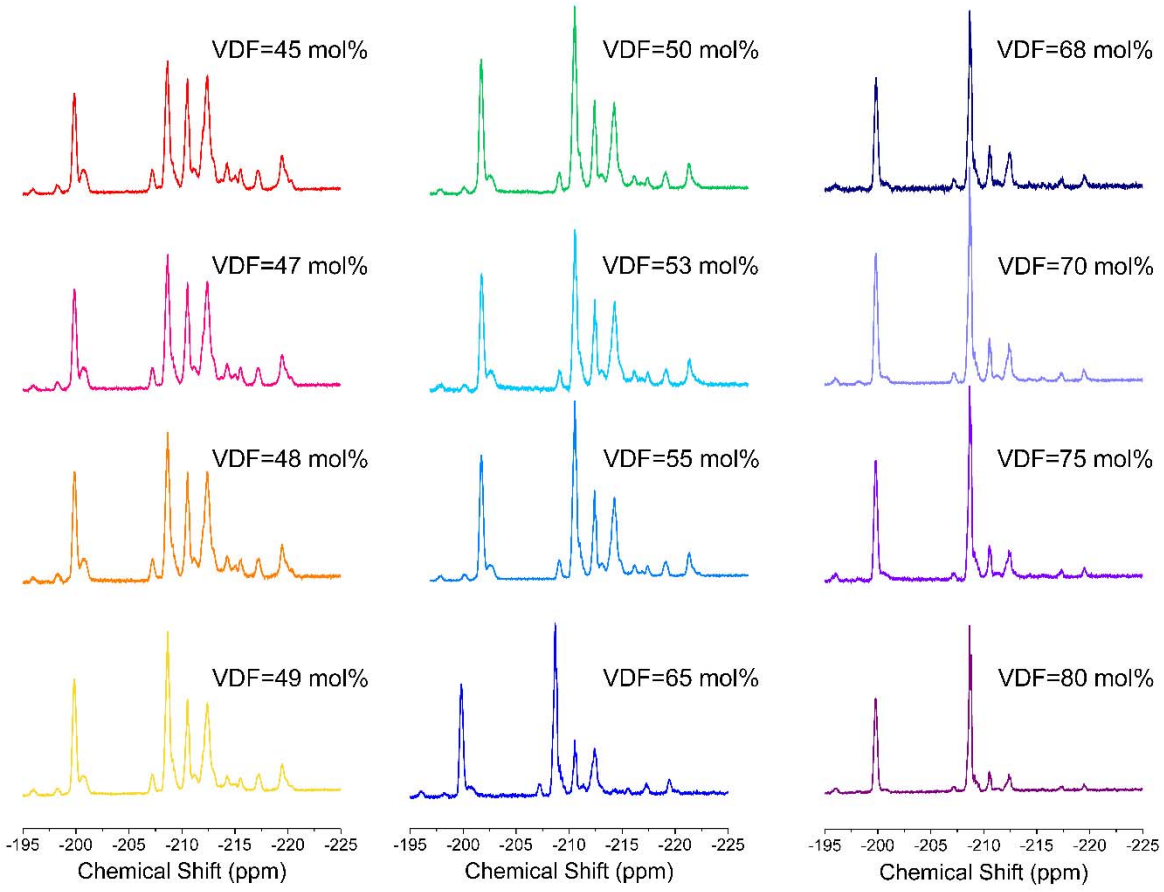

Figure S3. ^{19}F NMR spectra of the P(VDF-TrFE) copolymers in the region between -195 and -225 ppm.

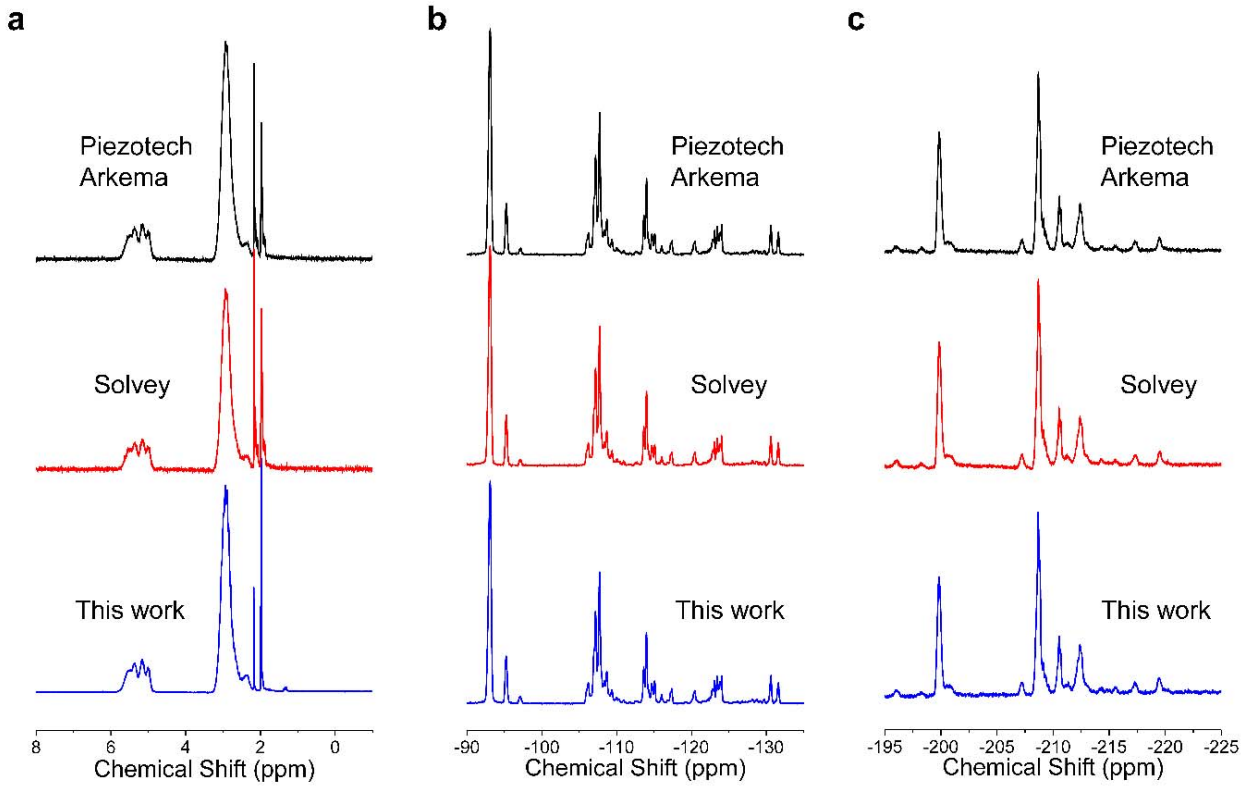

Figure S4. NMR spectra of the synthesized and commercial P(VDF-TrFE) 65/35 mol%. a, ^{1}H NMR spectra. **b**, **c** ^{19}F NMR spectra.

Table S1 Comparison of regio- and stereo-sequences between the synthesized and commercial copolymers of P(VDF-TrFE) 65/35 mol%

Sequence	Piezoetch Arkema	Solvey	This work
Regio-sequences			
VDF-VDF H-T	0.249	0.250	0.233
VDF-TrFE H-T	0.338	0.342	0.324
TrFE-TrFE H-T	0.204	0.205	0.223
H-T in total	0.791	0.797	0.780
H-H/T-T or T-T/H-H	0.068	0.066	0.071
Others	0.141	0.137	0.149
Stereo-sequences			
VDF-TrFE			
rr	0.893	0.886	0.880
mm	0.007	0.006	0.007
rm+mr	0.100	0.108	0.113
TrFE-TrFE			
rr	0.602	0.598	0.579
mm	0.224	0.226	0.235
rm+mr	0.174	0.176	0.186

H: head; T: tail. The steriosequences were calculated by measuring the ratios of the integral intensities of the respective triad peaks in the -CHF- resonance region of ^{19}F NMR spectra: For VDF-TrFE segment, the syndiotactic (rr), heterotactic (mr+rm), and isotactic (mm) triad peaks center at -199.9, -200.8, and -198.3 ppm, respectively; For TrFE-TrFE segment, the syndiotactic (rr), heterotactic (mr+rm), and isotactic (mm) triad peaks center at -208.7, -210.5, and -212.4 ppm, respectively.

2. Dynamic mechanical analysis of P(VDF-TrFE)s

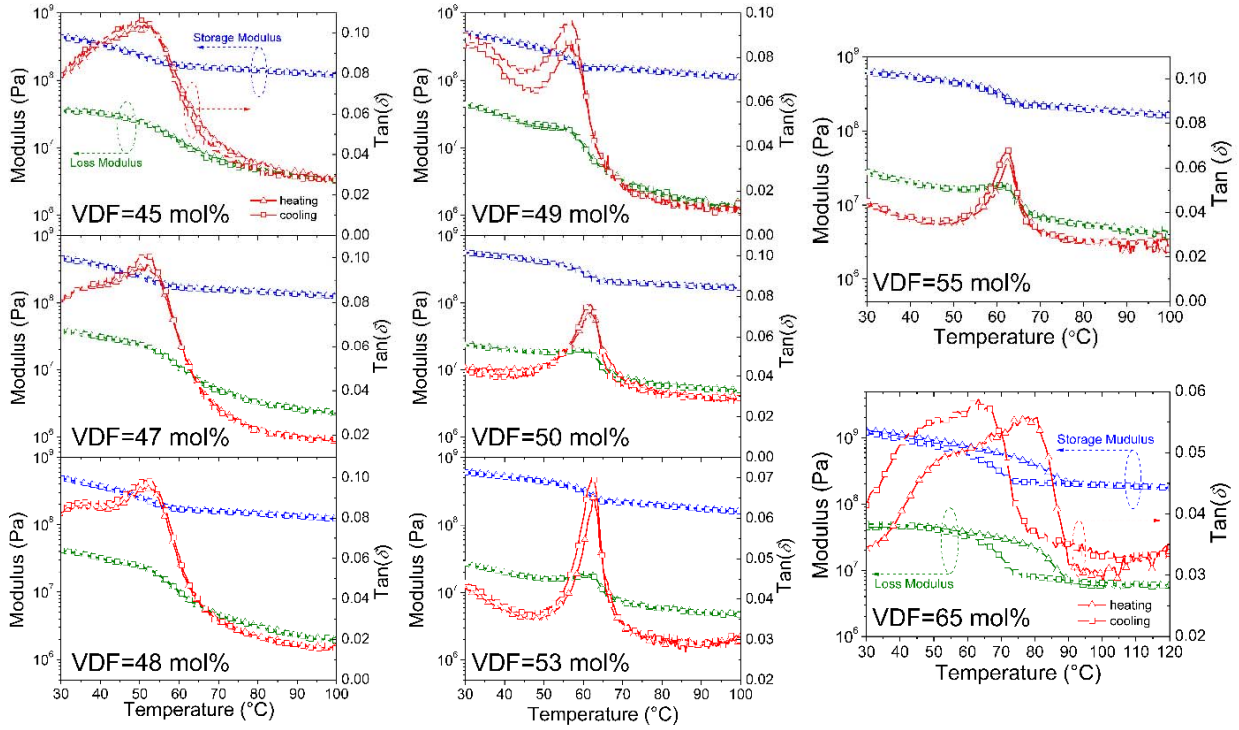

Figure S5. Dynamic mechanical analysis of P(VDF-TrFE) copolymers. Temperature dependence of storage modulus, loss modulus and loss tangent (defined as the ratio of the loss modulus to the storage modulus) upon heating and cooling of P(VDF-TrFE)s with different VDF contents.

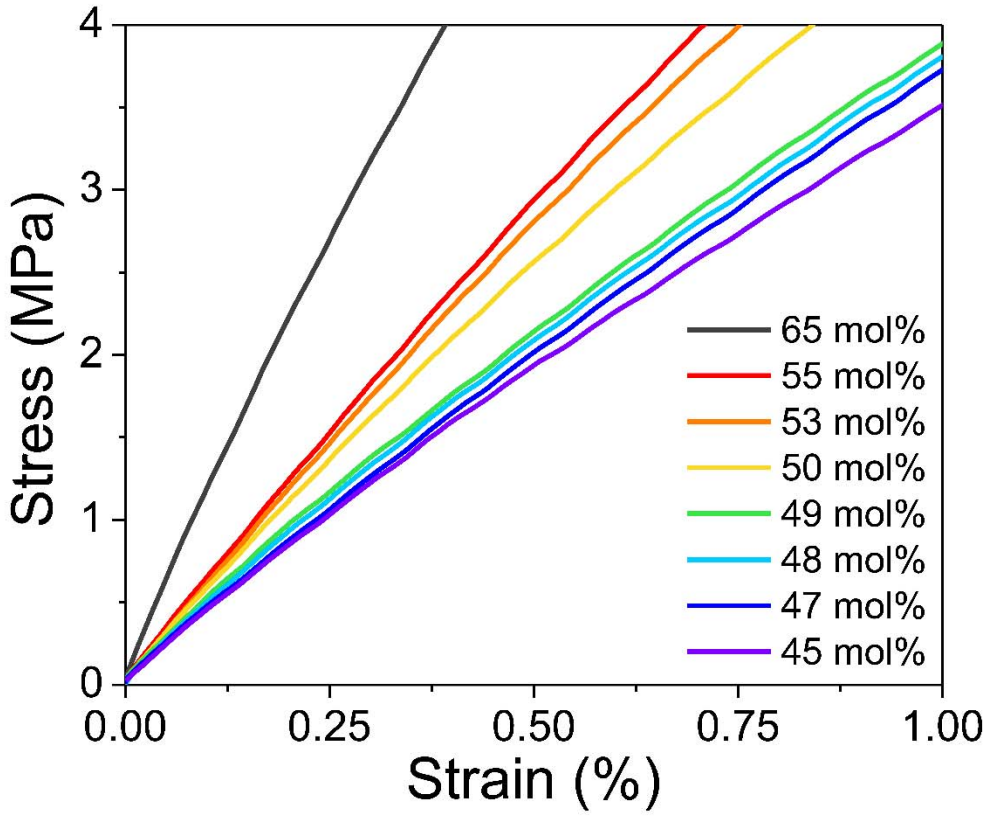

Figure S6. Stress-strain curve measured from tensile testing in P(VDF-TrFE) copolymers at room temperature.

3. X-ray diffraction (XRD) patterns and refinements

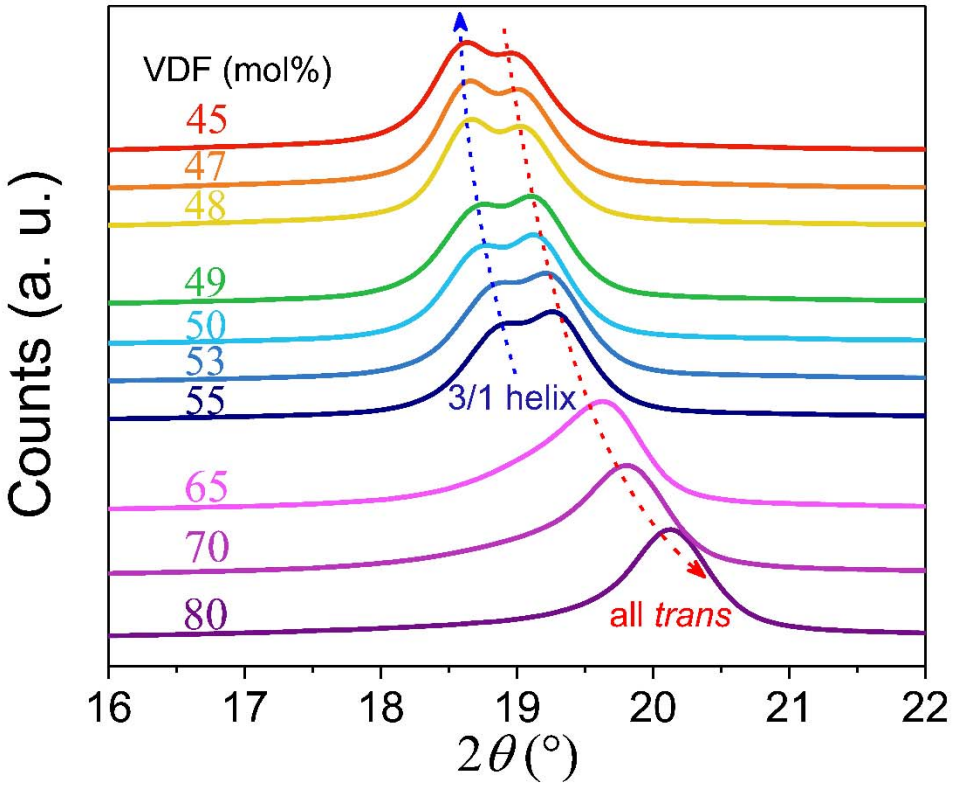

Figure S7. XRD θ-2θ scans of P(VDF-TrFE) copolymers. The dashed red line indicates the intensity growth of the *trans*-planar phase with increasing VDF content. The dashed blue line indicates the intensity growth of the 3/1-helical phase with decreasing VDF content.

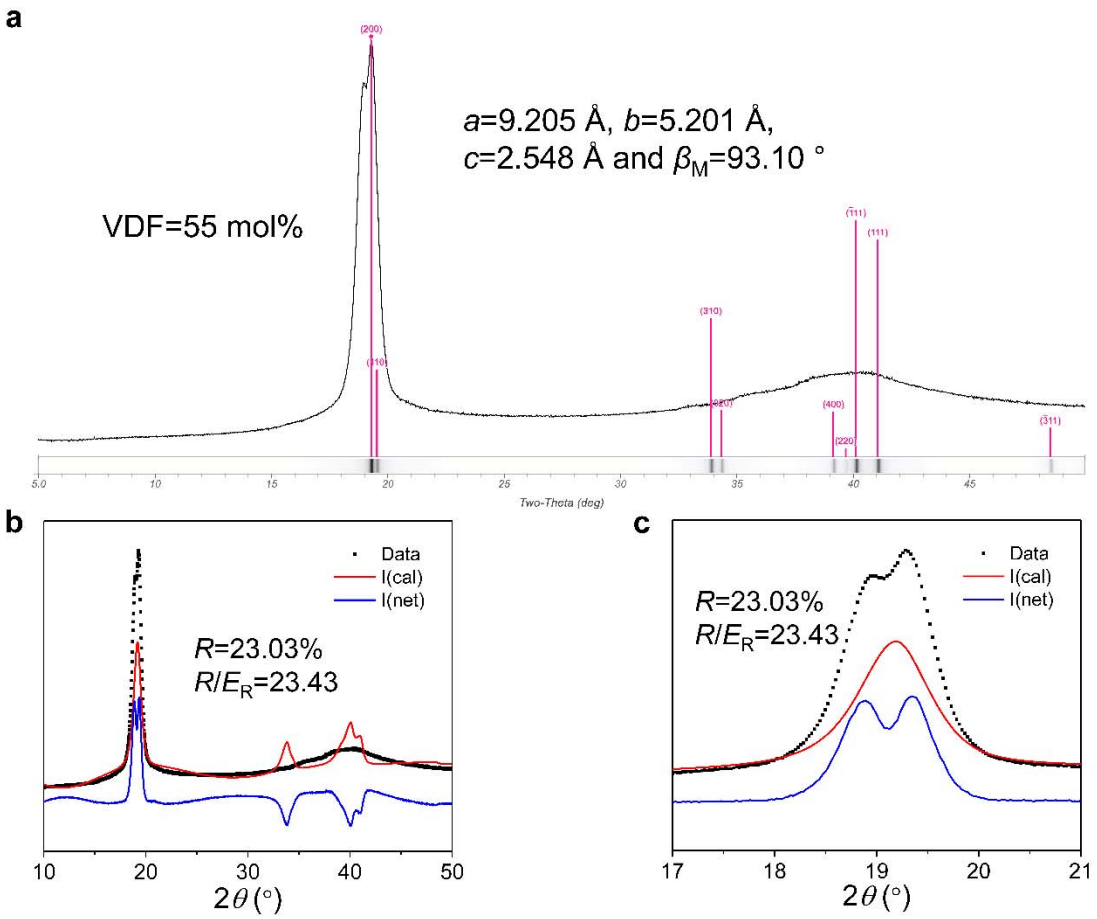

Figure S8. Rietveld analysis of P(VDF-TrFE) 55/45 mol% considering chain deflection. a, Comparison between the calculated and observed XRD pattern. **b**, **c**, Refinement results. The poor fitting results lead to a large agreement factor *R*=23.03%.

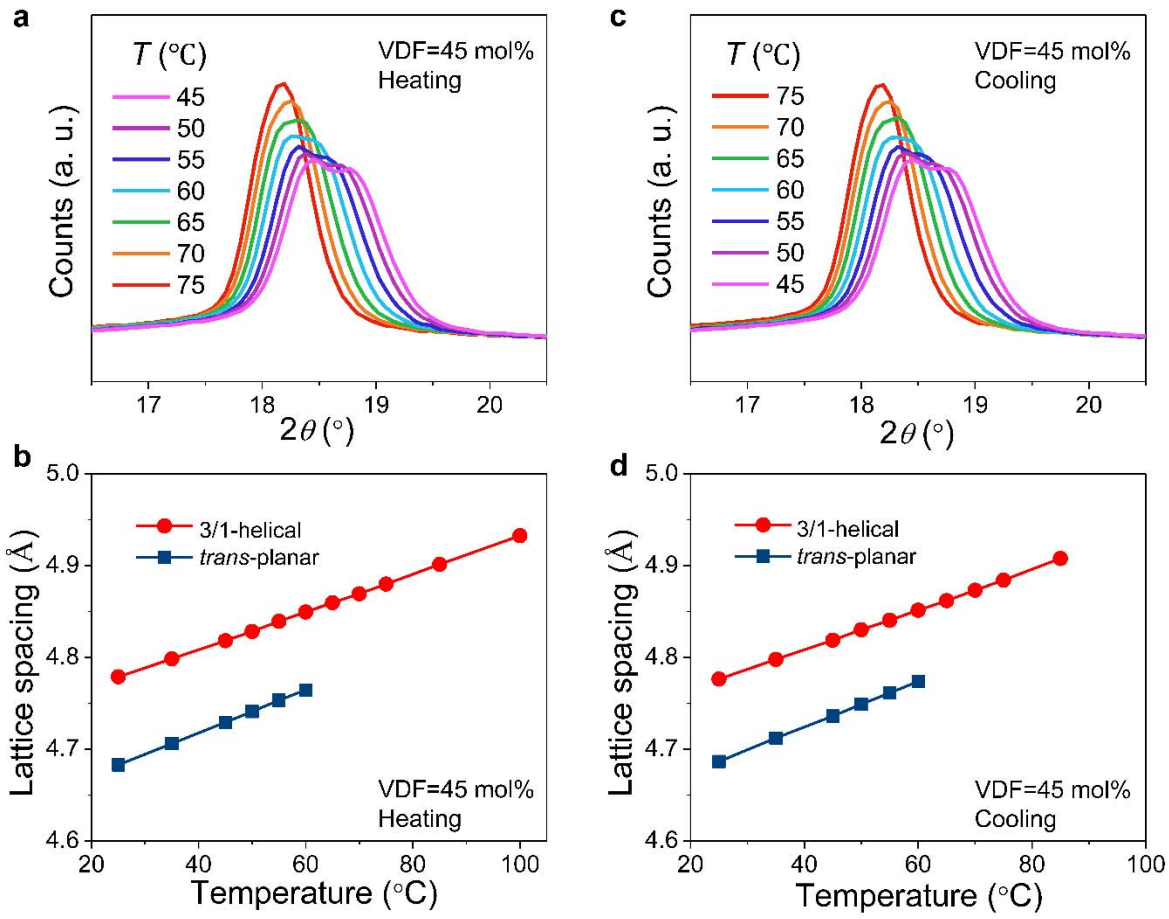

Figure S9. Temperature-dependent XRD patterns of P(VDF-TrFE) 45/55 mol%. a, **b**, Temperature dependence of the reflection pattern and the intermolecular spacing upon heating, respectively. **c**, **d**, Temperature dependence of the reflection pattern and the intermolecular spacing upon cooling, respectively.

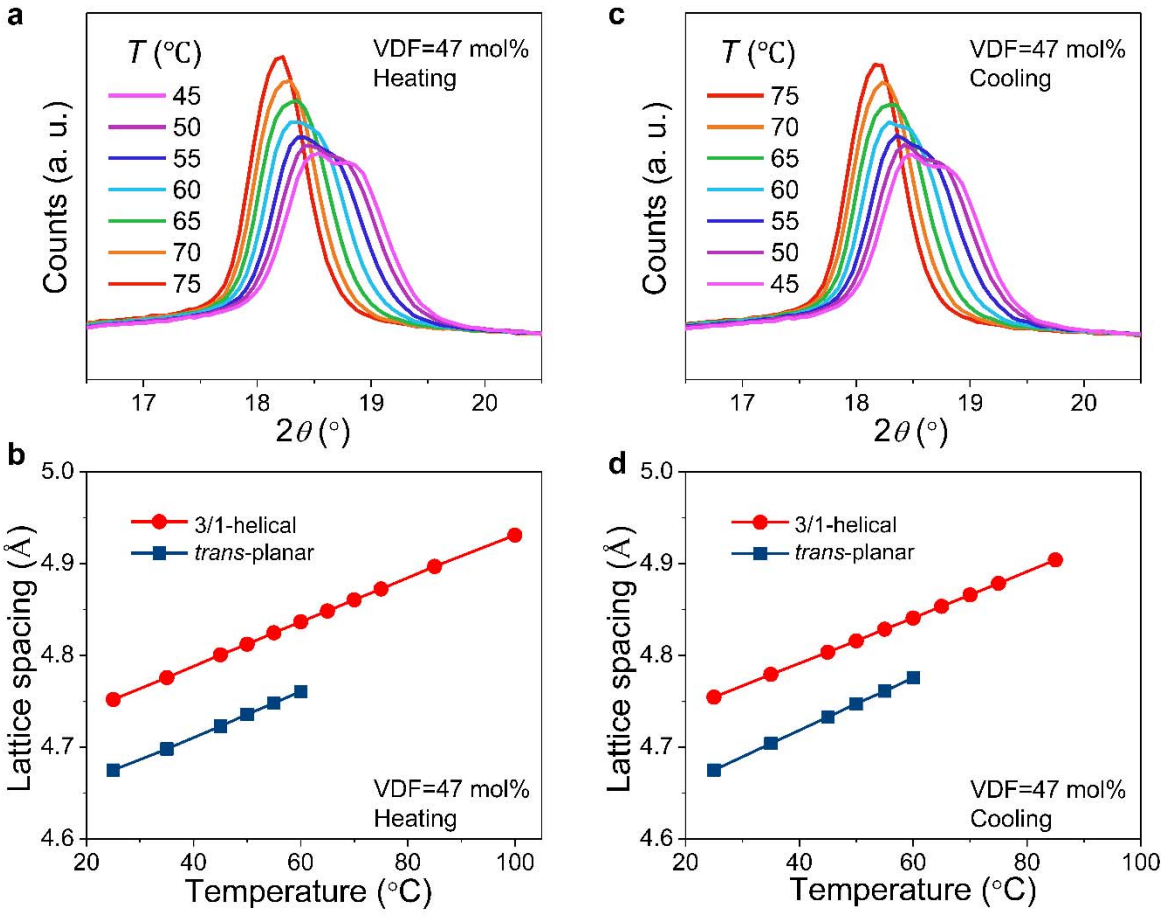

Figure S10. Temperature-dependent XRD patterns of P(VDF-TrFE) 47/53 mol%. a, **b**, Temperature dependence of the reflection pattern and the intermolecular spacing upon heating, respectively. **c**, **d**, Temperature dependence of the reflection pattern and the intermolecular spacing upon cooling, respectively.

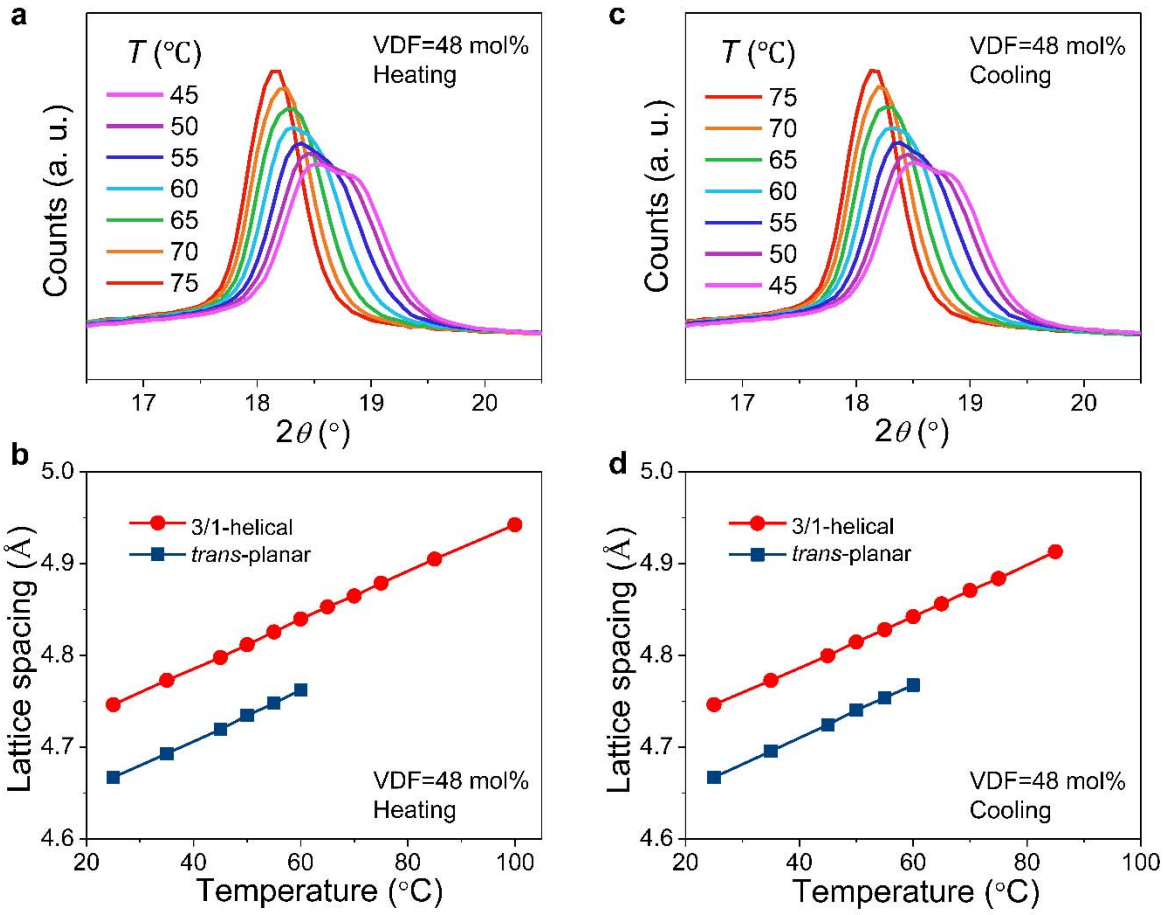

Figure S11. Temperature-dependent XRD patterns of P(VDF-TrFE) 48/52 mol%. a, **b**, Temperature dependence of the reflection pattern and the intermolecular spacing upon heating, respectively. **c**, **d**, Temperature dependence of the reflection pattern and the intermolecular spacing upon cooling, respectively.

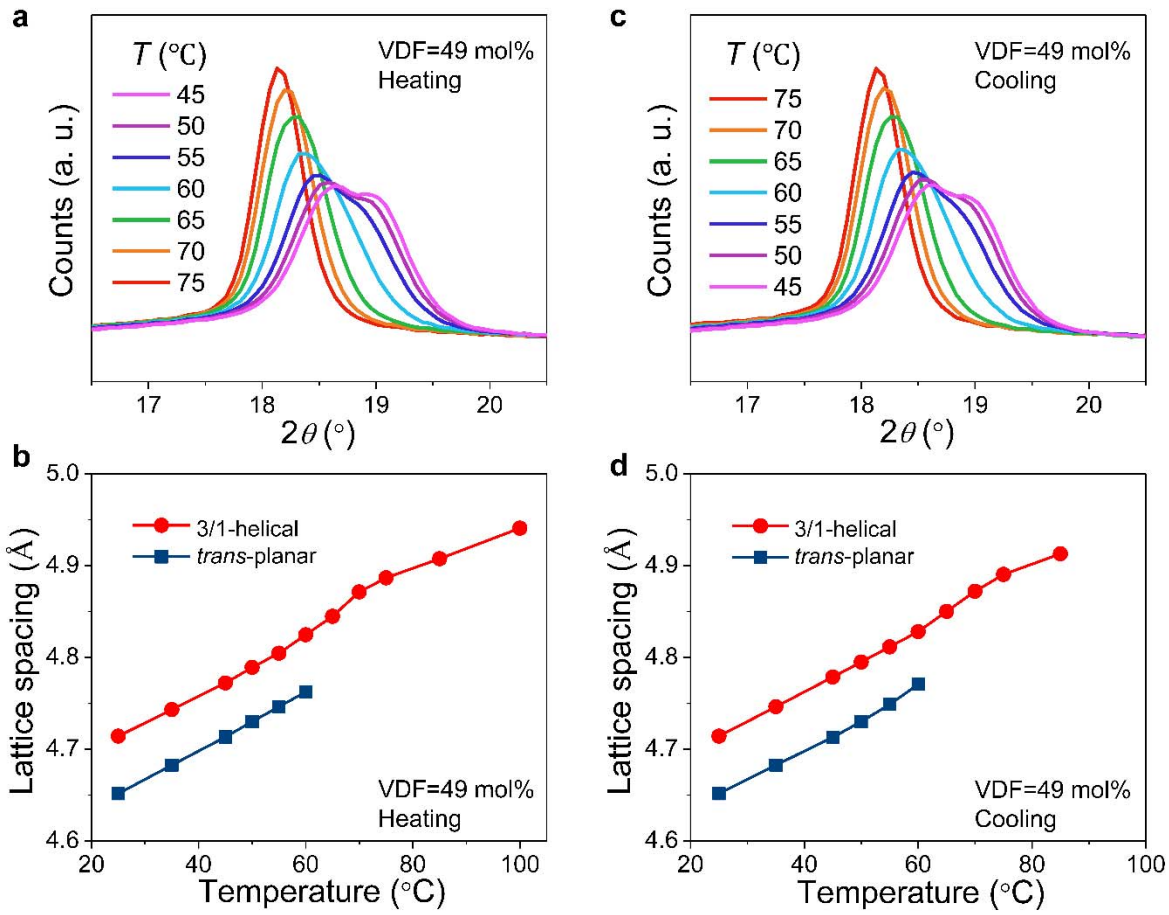

Figure S12. Temperature-dependent XRD patterns of P(VDF-TrFE) 49/51 mol%. a, **b**, Temperature dependence of the reflection pattern and the intermolecular spacing upon heating, respectively. **c**, **d**, Temperature dependence of the reflection pattern and the intermolecular spacing upon cooling, respectively.

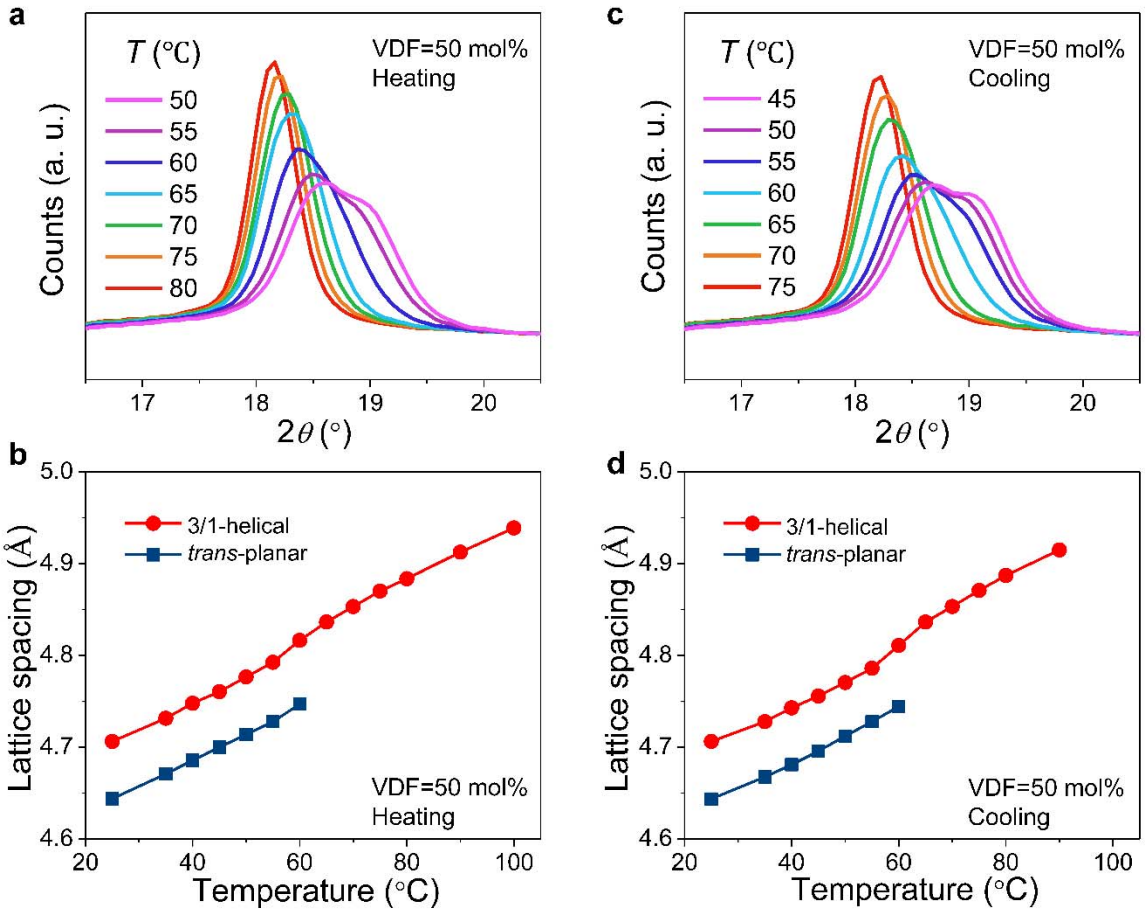

Figure S13. Temperature-dependent XRD patterns of P(VDF-TrFE) 50/50 mol%. a, **b**, Temperature dependence of the reflection pattern and the intermolecular spacing upon heating, respectively. **c**, **d**, Temperature dependence of the reflection pattern and the intermolecular spacing upon cooling, respectively.

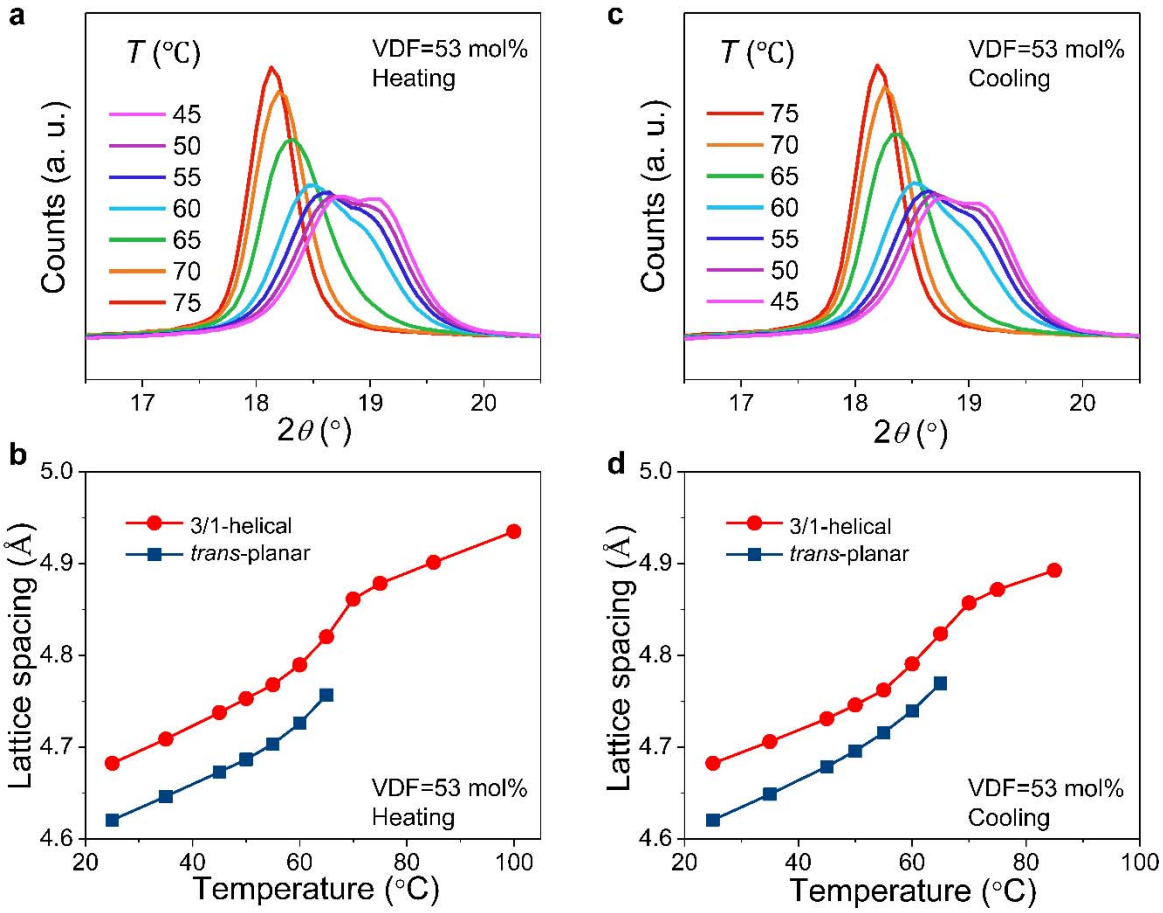

Figure S14. Temperature-dependent XRD patterns of P(VDF-TrFE) 53/47 mol%. a, **b**, Temperature dependence of the reflection pattern and the intermolecular spacing upon heating, respectively. **c**, **d**, Temperature dependence of the reflection pattern and the intermolecular spacing upon cooling, respectively.

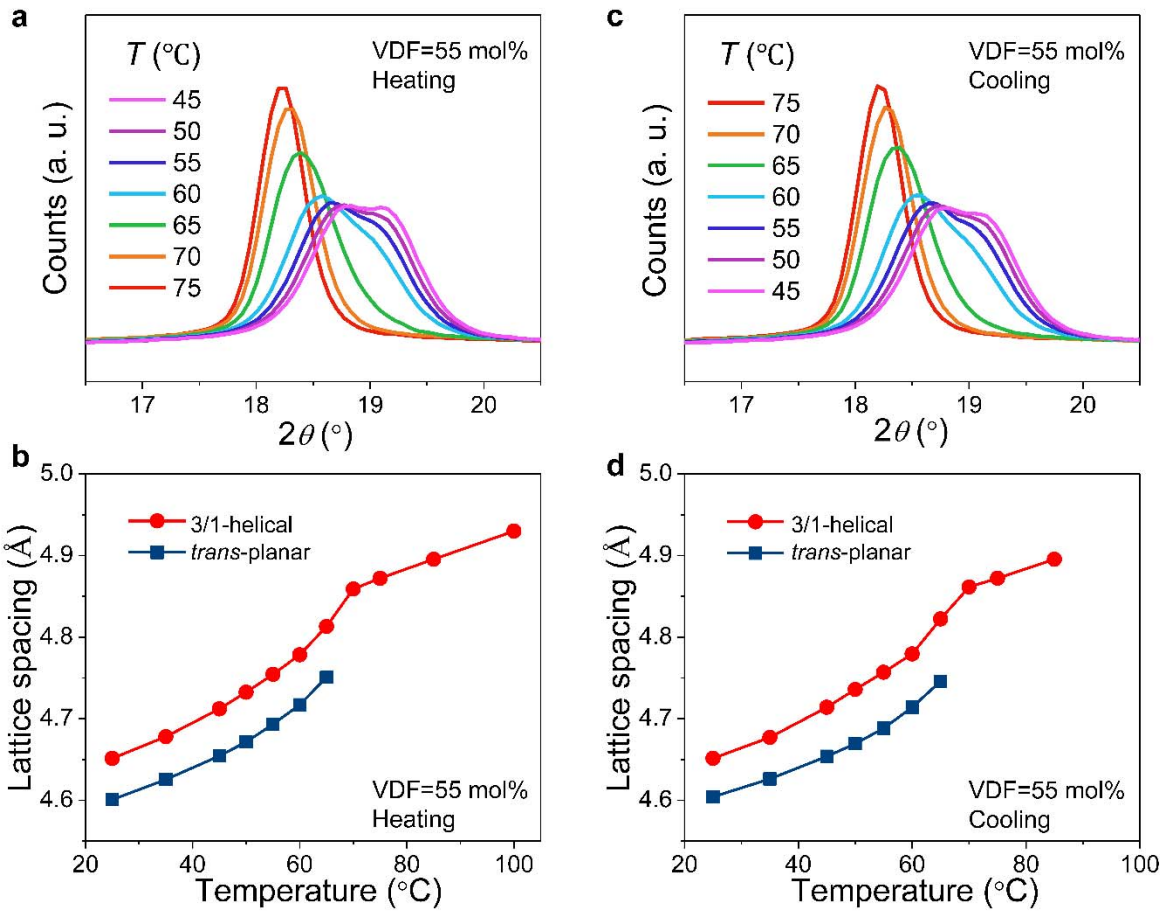

Figure S15. Temperature-dependent XRD patterns of P(VDF-TrFE) 55/45 mol%. a, **b**, Temperature dependence of the reflection pattern and the intermolecular spacing upon heating, respectively. **c**, **d**, Temperature dependence of the reflection pattern and the intermolecular spacing upon cooling, respectively.

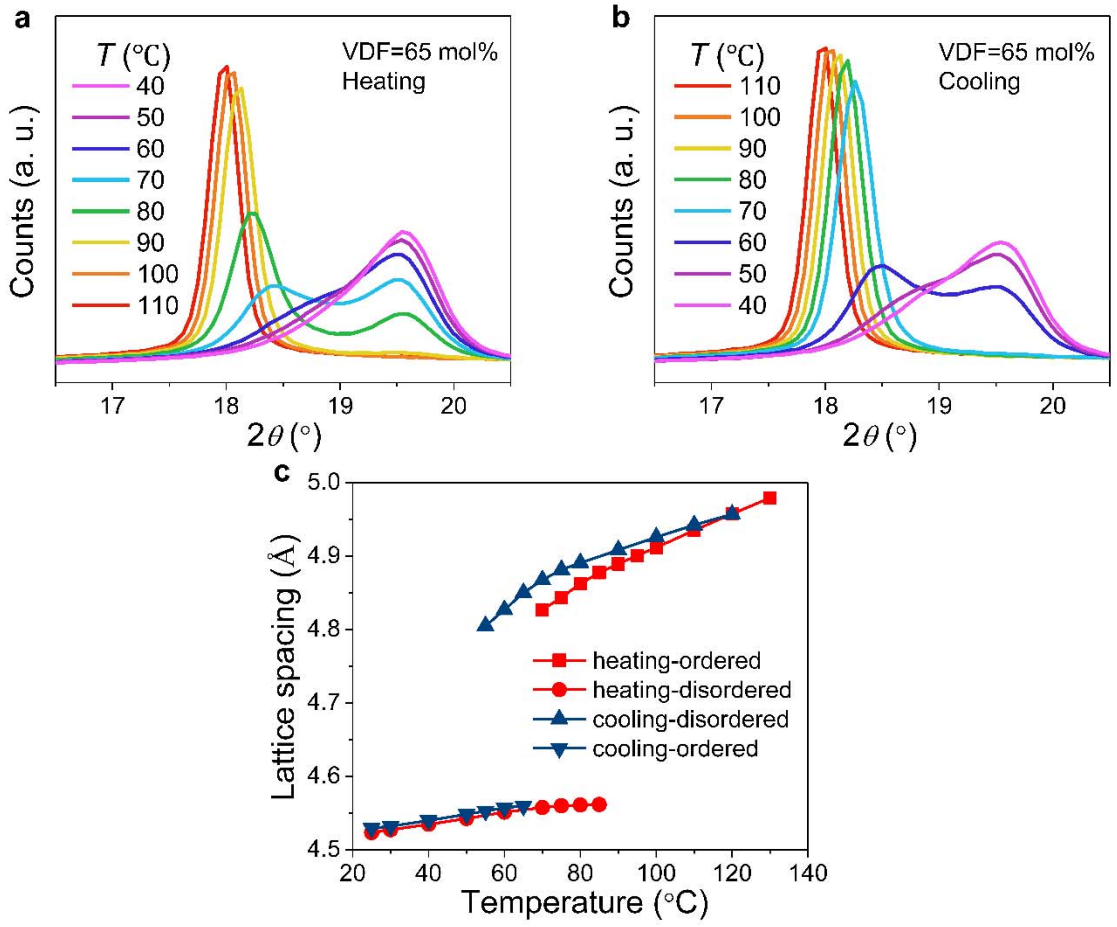

Figure S16. Temperature-dependent XRD patterns of P(VDF-TrFE) 65/35 mol%. a, **b**, Temperature dependence of the reflection pattern upon heating and cooling, respectively. **c**, Temperature dependence of the intermolecular spacing upon heating and cooling.

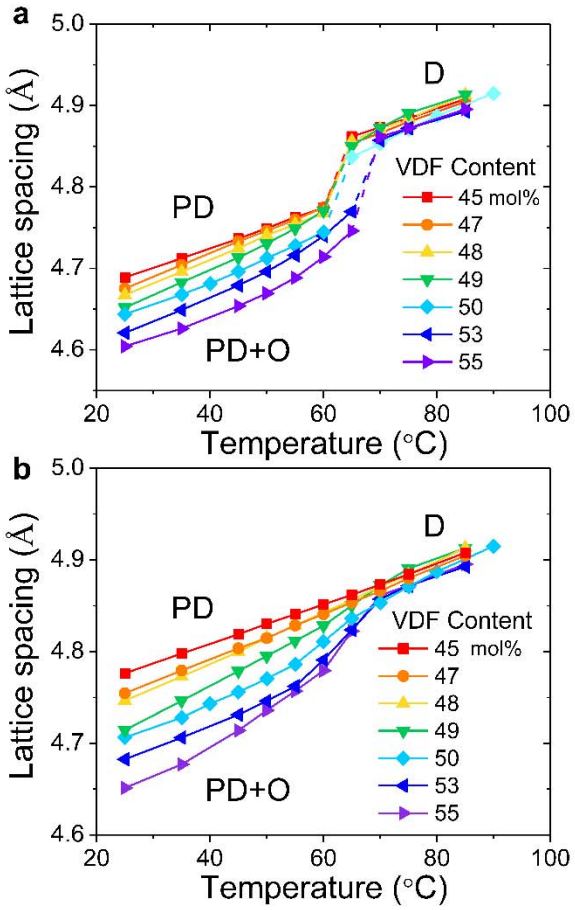

Figure S17. Temperature dependence of intermolecular spacings in P(VDF-TrFE) copolymers upon cooling. a, **b**, Intermolecular spacings of the *trans*-planar and 3/1-helical phases versus temperature upon cooling. O, D, and PD represent the ordered, disordered, and pseudo-disordered regions, respectively. The dashed lines shown in **a** indicate that the doublet merges into a singlet.

4. Fourier-transform infrared (FTIR) spectra

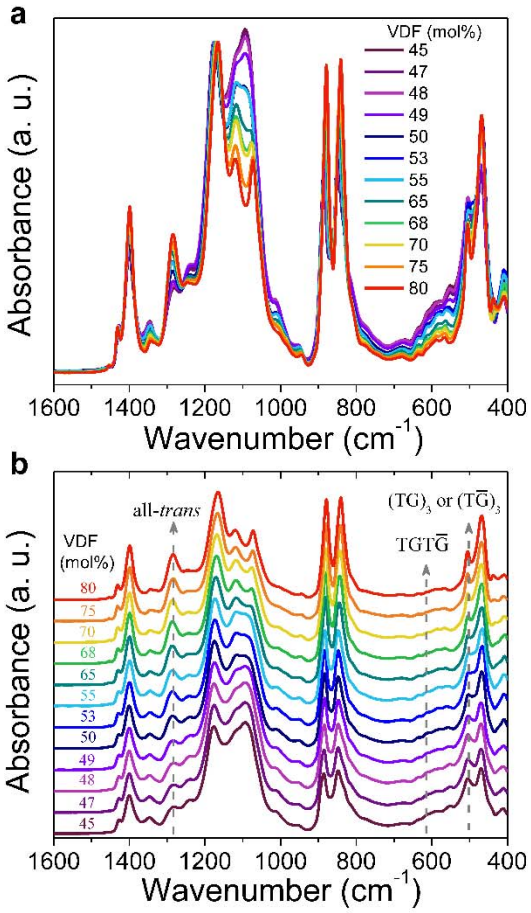

Figure S18. FTIR spectra of P(VDF-TrFE) copolymers with different VDF contents. a, Raw data. **b**, Offset adjustment of different spectra to give a better view. The grey dashed arrows mark the characteristic peaks of the all-*trans* conformation at about 1290 cm^{-1}, TGTḠ conformation at about 614 cm^{-1} and $(TG)_3$ or $(T\bar{G})_3$ conformation at about 507 cm^{-1}, respectively.

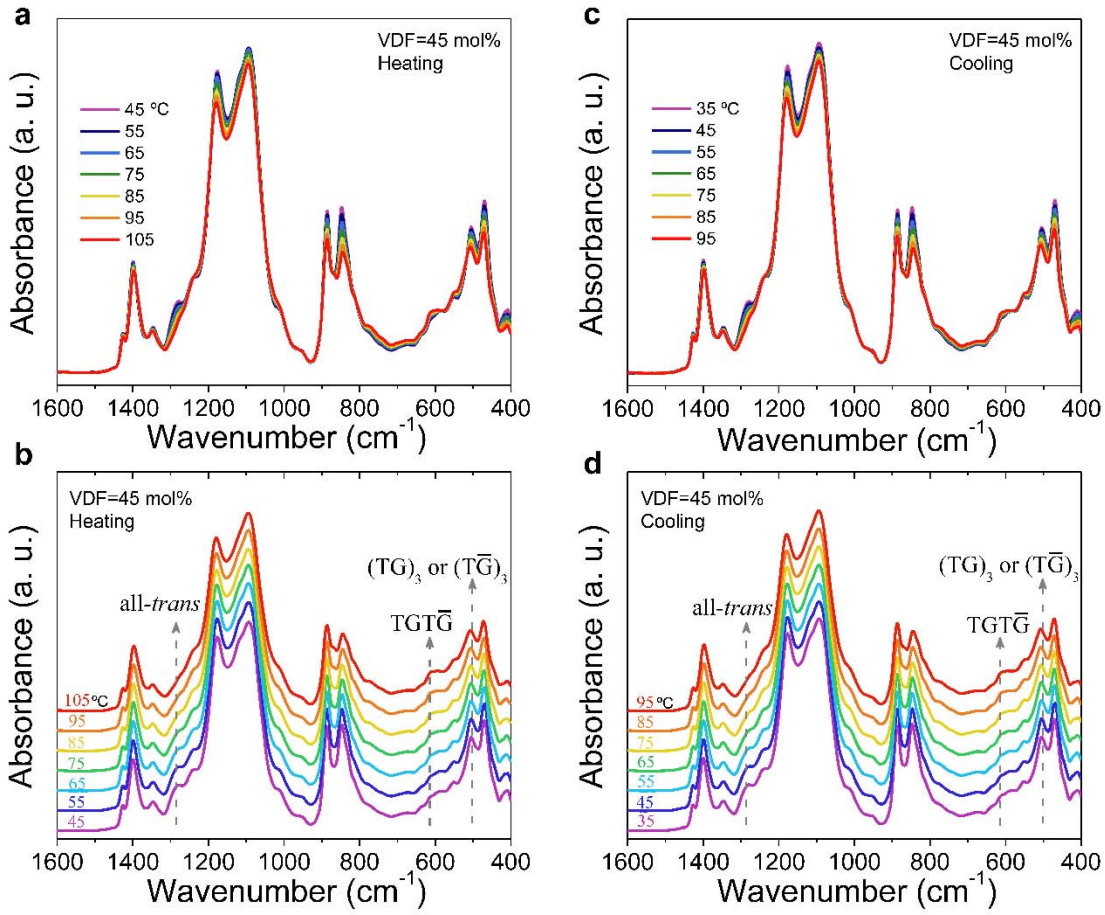

Figure S19. Temperature-dependent FTIR spectra of P(VDF-TrFE) 45/55 mol%. a-b and **c-d** correspond to heating and cooling, respectively. **a**, **c**, Raw data. **b**, **d**, Offset adjustment of different spectra to give a better view. The grey dashed arrows mark the characteristic peaks of the all-*trans* conformation at about 1290 cm^{-1}, TGTḠ conformation at about 614 cm^{-1} and $(TG)_3$ or $(T\bar{G})_3$ conformation at about 507 cm^{-1}, respectively.

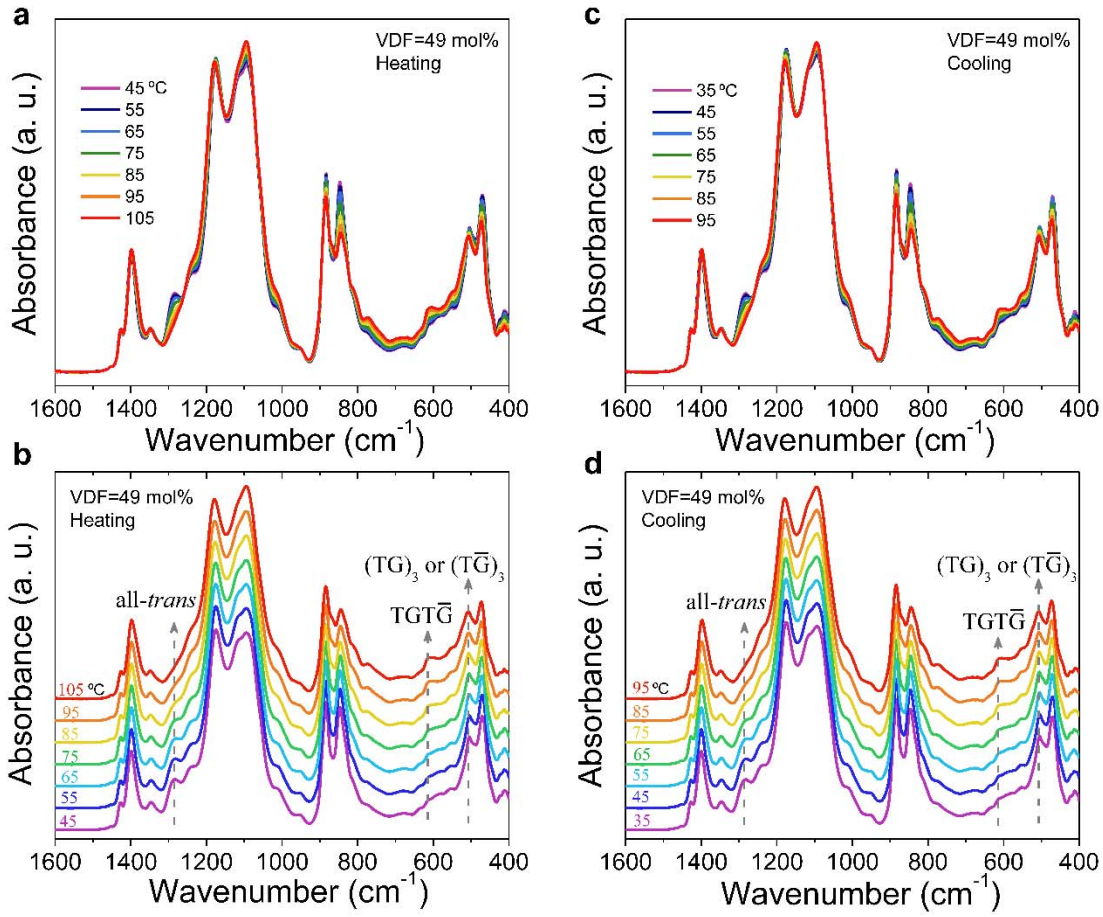

Figure S20. Temperature-dependent FTIR spectra of P(VDF-TrFE) 49/51 mol%. a-b and **c-d** correspond to heating and cooling, respectively. **a**, **c**, Raw data. **b**, **d**, Offset adjustment of different spectra to give a better view. The grey dashed arrows mark the characteristic peaks of the all-*trans* conformation at about 1290 cm^{-1}, TGTḠ conformation at about 614 cm^{-1} and $(TG)_3$ or $(T\bar{G})_3$ conformation at about 507 cm^{-1}, respectively.

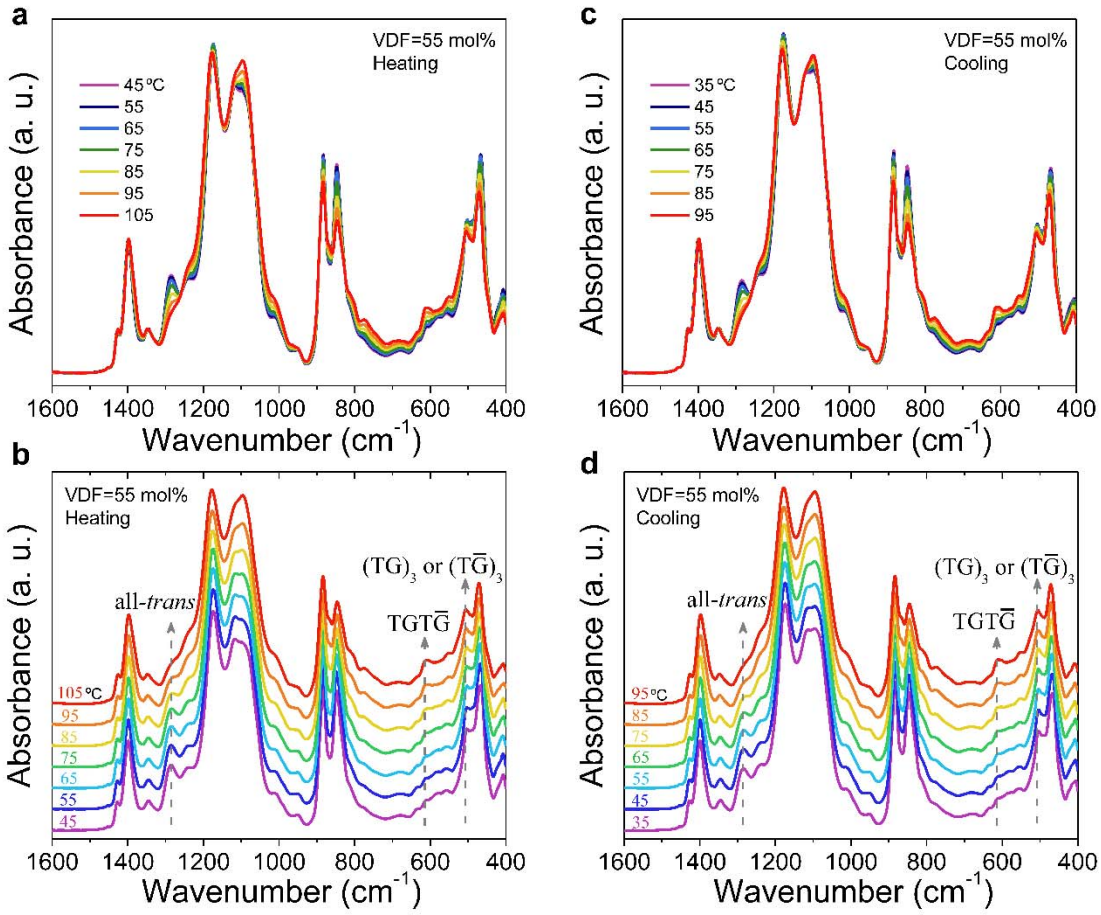

Figure S21. Temperature-dependent FTIR spectra of P(VDF-TrFE) 55/45 mol%. a-b and **c-d** correspond to heating and cooling, respectively. **a**, **c**, Raw data. **b**, **d**, Offset adjustment of different spectra to give a better view. The grey dashed arrows mark the characteristic peaks of the all-*trans* conformation at about 1290 cm^{-1}, TGTḠ conformation at about 614 cm^{-1} and $(TG)_3$ or $(T\bar{G})_3$ conformation at about 507 cm^{-1}, respectively.

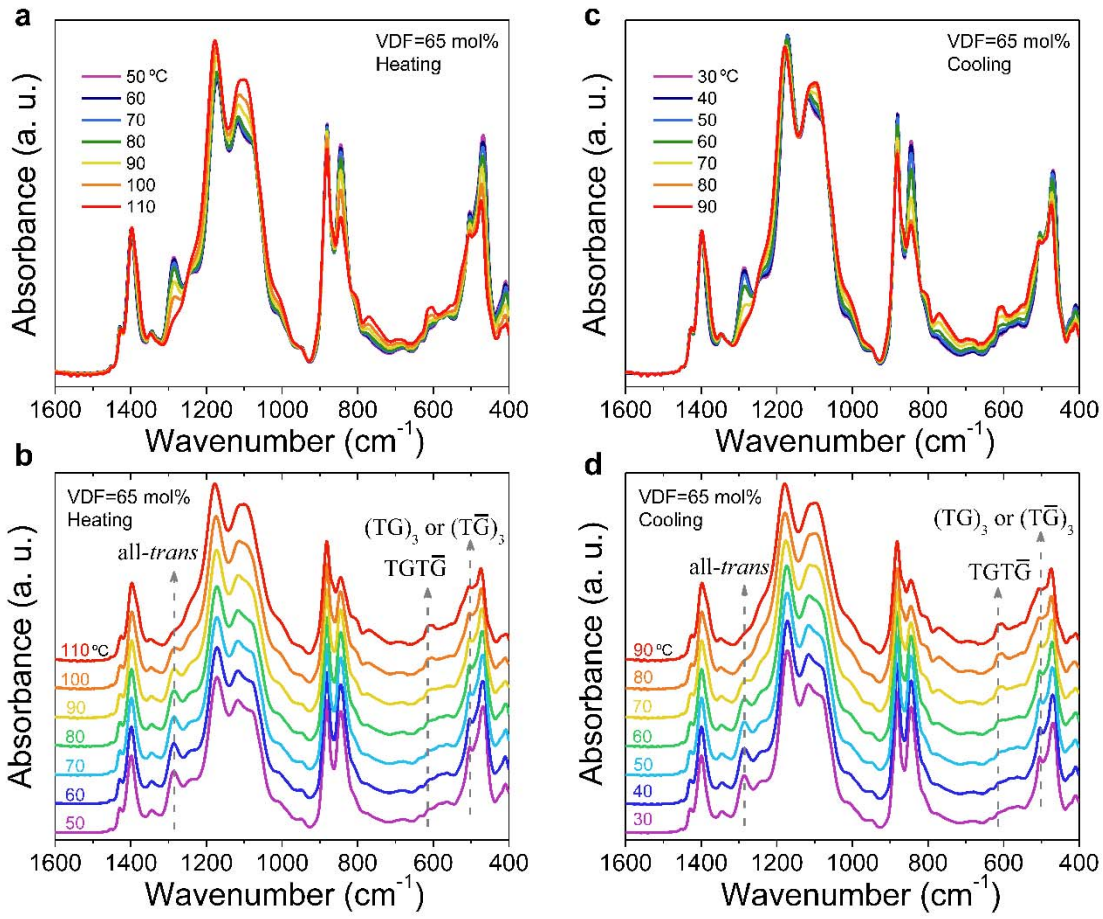

Figure S22. Temperature-dependent FTIR spectra of P(VDF-TrFE) 65/35 mol%. a-b and **c-d** correspond to heating and cooling, respectively. **a**, **c**, Raw data. **b**, **d**, Offset adjustment of different spectra to give a better view. The grey dashed arrows mark the characteristic peaks of the all-*trans* conformation at about 1290 cm^{-1}, TGTḠ conformation at about 614 cm^{-1} and $(TG)_3$ or $(T\bar{G})_3$ conformation at about 507 cm^{-1}, respectively.

6. Piezoelectric properties

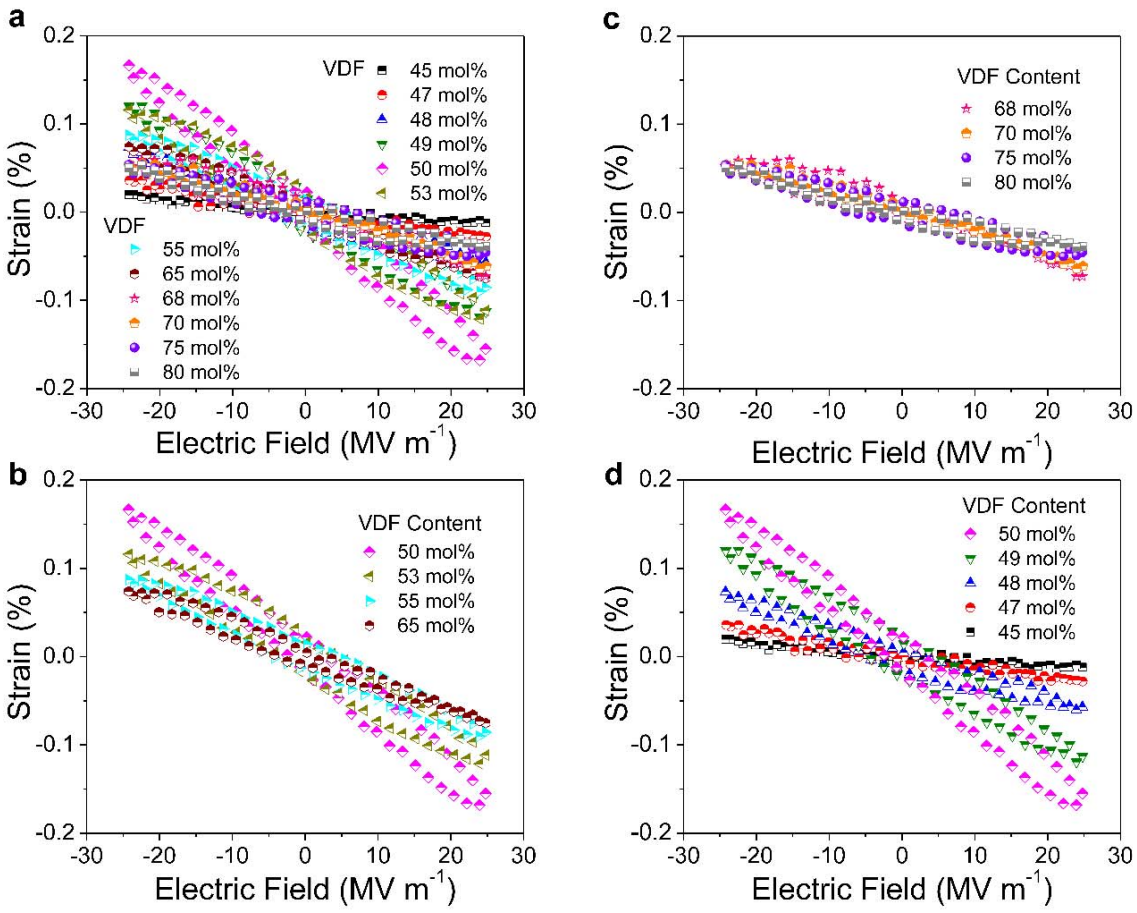

Figure S23. Piezoelectric properties of P(VDF-TrFE) copolymers at room temperature. a-d, Strain as a function of the applied electric field measured using a triangular ac electric field of 1 Hz. The measurement gives rise to an extracted d_{33} value of -29.1 ± 3 pC N^{-1} for VDF=65 mol% (1 Hz), which is in good agreement with previously reported data [-30.0 pC N^{-1} (0.1 Hz) in ref. S1 and -31.4 pC N^{-1} (1 Hz) in ref. S2].

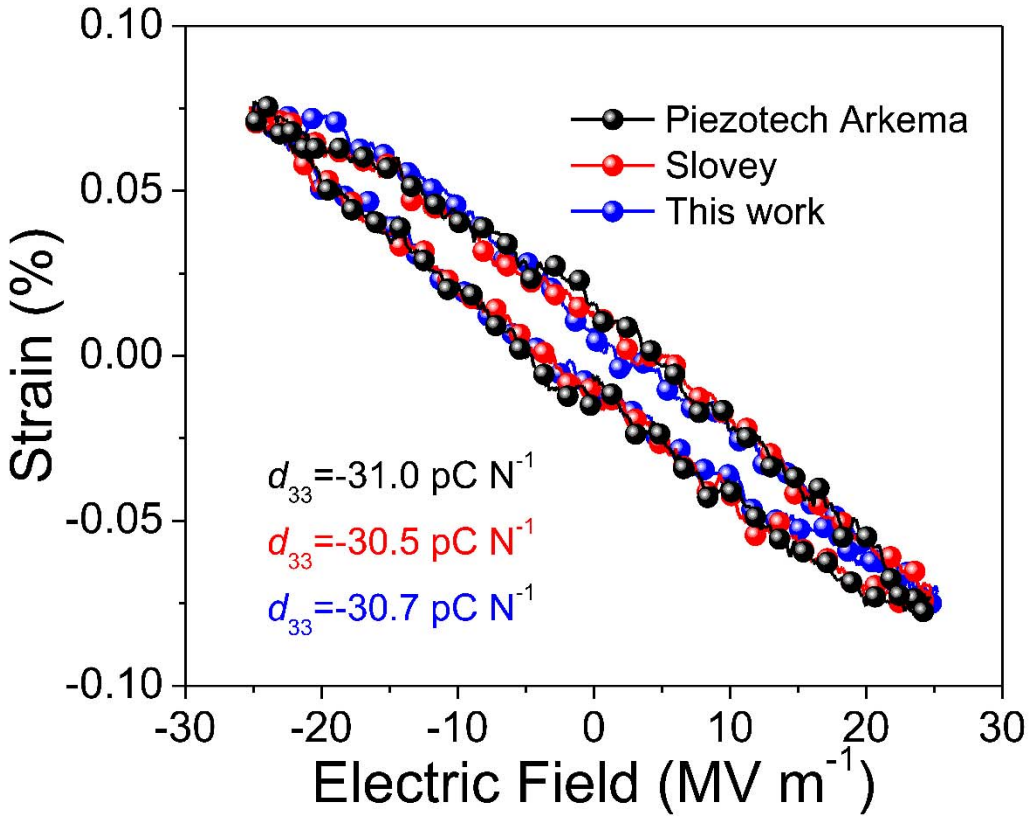

Figure S24. Piezoelectric responses of the synthesized and commercial P(VDF-TrFE) (65/35 mol%) purchased from Piezoetch Arkema and Solvey. We observe that all three P(VDF-TrFE) films display the same d_{33} value of ~-30 pC N^{-1}as shown in the piezoelectric strain – electric field measurements.

Table S2. Comparison of PVDF-based polymers with other typical piezoelectric polymers

Material	Thickness (μm)	d_{33} (pC N^{-1})	Reference
PVDF-based polymers			
Drawn PVDF	10-30	-26.0	[S1]
Spincoated PVDF	0.45	-37.7	[S2]
Undrawn P(VDF-TrFE) 81/19mol%	19-22	-18.0	[S3]
Drawn P(VDF-TrFE) 75/25mol%	20-80	-38.0	[S4]
Spincoated P(VDF-TrFE) 75/25mol%	0.05	-21.9	[S5]
LB[#] P(VDF-TrFE) 70/30mol%	0.015	-22.0	[S6]
Ultrathin P(VDF-TrFE) 70/30mol%	0.004	-46.4[†]	[S7]
Drawn P(VDF-TrFE) 65/35mol%	10-30	-35.0	[S1]
Undrawn P(VDF-TrFE) 65/35mol%	10-30	-30.0	[S1]
Spincoated P(VDF-TrFE) 65/35mol%	0.45	-31.4	[S2]
Drawn P(VDF-TrFE) 52/48mol%	---	-28.0	[S8]
Undrawn P(VDF-TrFE) 52/48mol%	10-30	-44.0	[S1]
Undrawn P(VDF-TrFE) 52/48mol%	20	-30.0	[S9]
Undrawn P(VDF-TrFE) 50/50mol%	60	**-63.5**	This work
Other semicrystalline polymers			
Nylon 11	30-35	-3.9	[S10]
Nylon 13	30-35	-4.1	[S10]
Parylene-C	50	-2.0	[S11]
Polyurea	0.5	10.0 (d_{31}[‡])	[S12]
Amorphous piezoelectric polymers			
Polyimide (β-CN)APB/ODPA[a)]	30	-16.5	[S13]
Polyimide (β-CN)APB/ODPA	---	-2.7	[S14]
Polyvinyl chloride (PVC)	1000	-1.0	[S15]
P(VDCN/VAc)[b)]	---	5.0 (d_{31}[‡])	[S16]
P(AN-MA)[c)]	10-15	3.0 (d_{31}[‡])	[S17]
Poly(meth)acrylate	---	1.5 (d_{31}[‡])	[S18]
Poly(1-bicyclobutanecarbonitrile)	25	0.3 (d_{31}[‡])	[S19]

[#] LB stands for Langmuir Blodgett.

[†] P(VDF-TrFE) is in the α phase in ref. S7 and its d_{33} (-46.4 pC N^{-1}) measured by piezoresponse force microscopy (PFM) corresponds to local effective piezoelectric coefficient rather than a bulk property that we focus on in our study.

[‡] d_{31} is the transverse piezoelectric coefficient. d_{31} was listed here because no d_{33} data were reported in these polymers.

[a)] Polyimide (β-CN)APB/ODPA: prepared from 2,6-bis(3-aminophenoxy) benzonitrile ((β-CN)APB) and 4,4' oxidiphthalic anhydride (ODPA).

[b)] P(VDCN/Vac): poly(vinylidene cyanide-*alt*-vinyl acetate)

[c)] P(AN-MA): poly(acrylonitrile-*co*-methyl acrylate)

7. Comparison of the theoretical and experimental piezoelectric results

In this section, we discuss in detail the results shown in Extended Data Figure 7. To obtain the electrostrictive coefficients Q_{33}, the electric field (E) induced polarization (P) and strain (S_3) curves were collected simultaneously at room temperature, which are shown in Figure. 2a and Extended Data Figure 7a in the main text. At high VDF contents (e.g., VDF=55 mol%), a typical P-E loop with nonzero remnant polarization (Figure 2a) and a "butterfly"-like strain curve (Extended Data Figure 7a) are observed, signifying the existence of robust ferroelectricity. As VDF content decreases below 49 mol%, polarization hysteresis loops evolve from ferroelectric to antiferroelectric-like type (Figure. 2a), which is accompanied by a remarkable smearing of the butterfly peaks (*e.g.*, VDF=45 mol%, Extended Data Figure 7a). We note that the copolymers with antiferroelectric-like loops (VDF<49 mol%) are in a single relaxor phase rather than a true antiferroelectric phase[S20] because of the absence of the typical strain response characteristic of antiferroelectrics (Extended Data Figure 7a).

To analyze the electrostriction, we plot S_3-P curves in Extended Data Figure 7b by eliminating the electric field in Figure. 2a and Extended Data Figure 7a. We find that the electrostriction results are hysteretic for all compositions. Considering VDF≤55 mol%, the hysteretic curve is characterized by hysteretic and reversible parts. We use the reversible parts at high electric fields to extract Q_{33}, because the irreversible parts at low fields may include extrinsic contributions from domain wall motions and domain switching. The existence of reversible parts for VDF≤55 mol% should be strongly related to the appearance of relaxor behavior for these compositions simply because it is known that relaxors typically exhibit reversible electrostrictive responses at high fields[S21,S22].

To extract Q_{33}, we plot S_3-P^2 curves, as shown in Extended Data Figure 7c. We show that the copolymers with typical morphotropic (49 mol%≤VDF≤55 mol%) and relaxor compositions (VDF<49 mol%) exhibit reversible electrostrictive responses at high fields (100 MV m^{-1}). With the decrease of VDF content, the slope of S_3-P^2 curves increases substantially (Extended Data Figure 7c). As a result, we summarize the extracted Q_{33} as a function of VDF content in Extended Data Figure 7d. We find a slope change at VDF=49 mol% (Extended Data Figure 7d), which is attributed to the disappearance of ferroelectric instability.

To gain insights into the origin of negative piezoelectricity in P(VDF-TrFE)s, we compare our experimental piezoelectric data with the theoretical models, as presented in Figure 2f in the main text. Interestingly, the relation $d_{33}/2Q_{33}\varepsilon_r\varepsilon_0P_r=1$ (where P_r is the remanent polarization, and ε_r and ε_0 are the relative and vacuum permittivities, respectively) is satisfied for the MPB compositions (49 mol%≤VDF≤55 mol%), which indicates that the electrostriction model can well account for negative longitudinal piezoelectric effect in P(VDF-TrFE)s. The good agreement between the electrostriction model and the experimental data explicitly demonstrates that crystalline and amorphous electromechanical coupling[S2] plays a negligible role in driving the negative piezoelectricity. Although a similar experimental agreement with the equation $d_{33}=2Q_{33}\varepsilon_r\varepsilon_0P_r$ was reported in ref. S1, the electrostriction was attributed to the dimensional effect arising from amorphous regions rather than the crystalline regions of P(VDF-TrFE)s. Recalling that electrostriction occurs in both crystalline and amorphous regions[S23], we note that the formula $d_{33}=2Q_{33}\varepsilon_r\varepsilon_0P_r$ generally works for normal ferroelectrics[S24] in which ferroelectricity arises only from the crystalline regions. Its validity in P(VDF-TrFE)s therefore rules out the contributions from the amorphous regions[S2].

Moreover, we have measured the composition dependence of the Young's modulus Y (Extended Data Figure 7e) to calculate the d_{33} according to the dimensional model[S25,S26] ($d_{33}\approx -P_r/Y$). The compositional evolution of Y in Extended Data Figure 7e reveals the existence of an intermediate transition region (49 mol%≤VDF≤55 mol%). More importantly, we show that the calculated d_{33} based on the dimensional effect are significantly larger in magnitude than the experimental ones. Such substantial deviations lead us to discard the interpretation of negative piezoelectricity in terms of the deformation accommodated by the amorphous part of P(VDF-TrFE)s[S25,26]. In addition, the Maxwell stress induced strain can be estimated through the relation $S_{Maxwell}=-1/2\varepsilon_r\varepsilon_0(S_{11}-2S_{12})E^2$ (ref. S27), in which S_{ij} is the elastic compliance. We find a negligible $|S_{Maxwell}|$ of 2.74×10^{-4} at 100 MV m^{-1}, which is more than one order of magnitude weaker than the electrostrictive strain of ~0.003-0.010 at the same field. Consequently, we conclude that the negative longitudinal piezoelectric effect originates from the electrostrictive effect in the crystalline regions of P(VDF-TrFE)s.

We also observe that the piezoelectric voltage coefficient g_{33} is significantly enhanced at MPB (49 mol%≤VDF≤55 mol%), as shown in Extended Data Figure 7f. The largest g_{33} of 0.394 V m N^{-1} is reached at VDF=50 mol%, which is nearly twice that (~0.20 V m N^{-1}) of the compositions (*i.e.* VDF=75 mol%) far away from MPB. We show in Extended Data Figure 7g that $2\varepsilon_r\varepsilon_0P_r$ can account well for the observed g_{33} within the MPB region, while the dimensional effect significantly overestimates the g_{33} values.

To justify electrostrictive coefficients measured at room temperature, further high-temperature measurements in the paraelectric phase are required to evaluate the contributions from ferroelectric switching and domain wall motion in ferroelectric phase. However, such a route is technically challenging for ferroelectric polymers that are limited by a lossy paraelectric phase,

especially at a lower frequency (*i.e.* 1 Hz) and a reduced breakdown field. The true Q_{33} cannot be reached in the case of a lossy paraelectric phase because of the extrinsic contributions from the dramatic increase of electrical conductivity, even though a S_3-P response is obtained. Here we overcome this technical challenge by successfully measuring the high-temperature electrostrictive responses on the P(VDF-TrFE) with a typical MPB composition of 50/50 mol%, which exhibits the largest piezoelectric response (d_{33}=-63.5±3.2 pC N^{-1}) in piezoelectric polymers (Table S2). At 70 ºC (just above the Curie temperature of ~65 ºC), a slim polarization loop is shown in Extended Data Figure 7h, signifying the nearly loss-free paraelectric phase. The strain-field curve evolves from a typical butterfly at 25 ºC into a shape characterized by remarkably flatter butterfly peaks at 70 ºC (Extended Data Figure 7i), which is due to an order-disorder phase transition. As expected, the hysteresis in S_3-P curve at 70 ºC is reduced considerably compared to that at 25 ºC (Extended Data Figure 7j). Moreover, the slope of the S_3-P^2 curve measured at 70 ºC changes only slightly with respect to that obtained at 25 ºC (Extended Data Figure 7k): Q_{33} extracted at 70 ºC is -4.18±0.32 m^4 C^{-2} while it is -3.68±0.21 m^4 C^{-2} at 25 ºC. Consequently, the calculated d_{33} is -68.3 pC N^{-1} using a Q_{33} value of -4.18 m^4 C^{-2}, which is slightly larger than the experimental one (-63.5±3.2 pC N^{-1}). In addition, we find that the copolymer at relatively low electric fields (e.g., 25 MV m^{-1}) only displays the typical quadratic behavior response to the electric field that is characteristic of electrostriction at 70 ºC. The magnitude of the electrostrictive strain at 25 MV m^{-1} is slightly higher than the piezoelectric strain measured at 25 ºC (Extended Data Figure 7l). This provides clear evidence of non piezoelectric nature of the paraelectric phase, in contrast to previous results,[S28,S29] and shows that robust piezoelectricity still exists just above the Curie temperature. In short, our high temperature electrostrictive results unambiguously support our foregoing conclusion that electrostriction with a negative sign in the crystalline regions with a negative sign

is the origin of negative longitudinal piezoelectric effect in P(VDF-TrFE)s.

In summary, we have determined the electrostrictive coefficients of P(VDF-TrFE)s with MPB compositions using electrostrictive measurements and revealed that the negative longitudinal piezoelectricity originates from the electrostriction in the crystalline part of P(VDF-TrFE)s, independent of amorphous regions and crystalline-amorphous interfaces.

8. References

S1. Furukawa, T. & Seo, N. Electrostriction as the origin of piezoelectricity in ferroelectric polymers. *Jpn. J. Appl. Phys.* **29**, 675-680 (1990).

S2. Katsouras, I., Asadi, K., Li, M., van Driel, T. B., Kjaer, K. S., Zhao, D., Lenz, T., Gu, Y., Blom, P. W. M., Damjanovic, D., Nielsen, M. M. & De Leeuw, D. M. The negative piezoelectric effect of the ferroelectric polymer poly (vinylidene fluoride). *Nat. Mater.* **15**, 78-84 (2016).

S3. Oliveira, F., Leterrier, Y., Månson, J.-A., Sereda, O., Neels, A., Dommann, A. & Damjanovic, D. Process influences on the structure, piezoelectric, and gas-barrier properties of PVDF-TrFE copolymer. *J. Polym. Sci. B Polym. Phys.* **52**, 496-506 (2014).

S4. Omote, K., Ohigashi, H. & Koga K. Temperature dependence of elastic, dielectric, and piezoelectric properties of "single crystalline" films of vinylidene fluoride trifluoroethylene copolymer. *J. Appl. Phys.* **81**, 2760-2769 (1997).

S5. Choi, Y.-Y., Sharma, P., Phatak, C., Gosztola, D. J., Liu, Y., Lee, J., Lee, B., Li, J., Gruverman, A., Ducharme, S. & S. Hong. Enhancement of local piezoresponse in polymer ferroelectrics via nanoscale control of microstructure. *ACS Nano* **9**, 1809-1819 (2015).

S6. Bune, A. V., Zhu, C., Ducharme, S., Blinov, L. M., Fridkin, V. M., Palto, S. P., Petukhova, N. G. & Yudin, S. G. Piezoelectric and pyroelectric properties of ferroelectric Langmuir-Blodgett polymer films. *J. Appl. Phys.* **85**, 7869-7873 (1999).

S7. Qian, J., Jiang, S., Wang, Q. J., Zheng, S. S., Guo, S. Y., Yi, C., Wang, J. P., Wang, X. R., Tsukagoshi, K., Shi, Y. & Li, Y. Unveiling the piezoelectric nature of polar α-phase P(VDF-TrFE) at quasi-two-dimensional limit. *Sci. Rep.* **8**, 532 (2018).

S8. Furukawa, T. & Wen, J. X. Electrostriction and piezoelectricity in ferroelectric polymers. *Jpn. J. Appl. Phys.* **23**, 677-679 (1984).

S9. Furukawa, T., When, J. X., Suzuki, K., Takashina, Y. & Date, M. Piezoelectricity and pyroelectricity in vinylidene fluoride/trifluoroethylene copolymers. *J. Appl. Phys.* **56**, 829-834 (1984).

S10. Liu, S., Cui, Z., Fu, P., Liu, M., Zhang, Y., Jia, R. & Zhao, Q. Piezoelectricity and ferroelectricity in odd-odd nylons with long alkane segments. *Appl. Phys. Lett.* **104**, 172906 (2014).

S11. Kim, J. Y., Cheng, A. & Tai. Y. Parylene-C as a piezoelectric material. *IEEE MEMS (Cancun)* 473-476 (2011). DOI: 10.1109/MEMSYS.2011.5734464

S12. Wang, X.-S., Iijima, M., Takahashi, Y. & Fukada, E. Dependence of piezoelectric and pyroelectric activities of aromatic polyurea thin films on monomer composition ratio. *Jpn. J. Appl. Phys*. **32**, 2768-2773 (1993).

S13. Park, C., Ounaies, Z., Wise, K. E. & Harrison, J. S. In situ poling and imidization of amorphous piezoelectric polyimides. *Polymer* **45**, 5417-5425 (2004).

S14. Simpson, J. O., Ounaies, Z. & Fay, C. Polarization and piezoelectric properties of a nitrile substituted polyimide. *Proc. Mater. Res. Soc. Symp.: Mater. Smart Syst. II* **459**, 59-64 (1997).

S15. Li, R., Zhou, J., Liu, H. & Pei, J. Effect of polymer matrix on the structure and electric properties of piezoelectric lead zirconatetitanate/polymer composites. *Materials* **10**, 945 (2017).

S16. Miyata, S., Yoshikawa, M., Tasaka, S. & Ko, M. Piezoelectricity revealed in the copolymer of vinylidene cyanide and vinyl acetate. *Polym. J.* **12**, 857-860 (1980).

S17. von Berlepsch, H., Kunstler, W., Wedel, A., Danz, R. & Geiss, D. Piezoelectric activity in a copolymer of acrylonitrile and methylacrylate. *IEEE Trans. Electr. Insul.* **24**, 357-362 (1989).

S18. Lee, J.-Y., Jin, M.-K. & Park, E.-J. Synthesis and characterization of poly(meth)acrylates containing tricyanocyclopropane ring for piezoelectric applications. *Polym. Bull.* **45**, 17-23 (2000).

S19. Hall, H. K., Chan, R. H., Oku, Hughes, O. R., Scheinbeim, J. & Newman, J. B. Piezoelectric activity in films of poly(1-bicyclobutanecarbonitrile). *Polym. Bull.* **17**, 135-136 (1987).

S20. Furukawa, T. & Takahashi, Y. Ferroelectric and antiferroelectric transitions in random copolymers of vinylidene fluoride and trifluoroethylene. *Ferroelectrics* **264**, 1739-1748 (2001).

S21. Jang, S. J., Uchino, K., Nomura, S. & Cross, L. E. Electrostrictive behavior of lead magnesium niobate based ceramic dielectrics. *Ferroelectrics* **27**, 31-34 (1980).

S22. Zhang, Q. M., Bharti, V. & Zhao, X. Giant electrostriction and relaxor ferroelectric behavior in electron-irradiated poly(vinylidene fluoride-trifluoroethylene) copolymer. *Science* **280**, 2101-2104 (1998).

S23. Jaffe, B., Cook, W. R. & Jaffe, H. Piezoelectric Ceramics (Academic, 1971).

S24. Lines, M. E. & Glass, A. M. Principles and Applications of Ferroelectrics and Related Materials (Oxford Univ. Press, 1977).

S25. Broadhurst, M. G., Davis, G. T., McKinney, J. E. & Collins, R. E. Piezoelectricity and pyroelectricity in polyvinylidene fluoride-a model. *J. Appl. Phys.* **49**, 4992-4997 (1978).

S26. Broadhurst, M. G. & Davis, G. T. Physical basis for piezoelectricity in PVDF. *Ferroelectrics* **60**, 3-13 (1984).

S27. Zhang, Q. M., Huang, C., Xia, F. & Su, J. Chapter 4: Electric Electroactive polymer (EAP), EAP actuators as artificial muscles: reality, potential, and challenges, edited by Y. Bar-Cohen (SPIE PRESS, Washington, 2004). All the parameters used are taken from the text book: ε_r=10, s_{11}=3.32×10^{-10} Pa^{-1}, s_{12}=-1.44×10^{-10} Pa^{-1}.

S28. Higashihata, Y., Sako, J. & Yagi, T. Piezoelectricity of vinylidene fluoride-trifluoroethylene copolymers. *Ferroelectrics* **32**, 85-92 (1981).

S29. Yamada, T. & Kitayama, T. Ferroelectric properties of vinylidene fluoride-trifluoroethylene copolymers. *J. Appl. Phys.* **52**, 6859-6863 (1981).